metals

MDPI

Article

Microstructure, Mechanical Properties, and Corrosion Behavior of 06Cr15Ni4CuMo Processed by Using Selective Laser Melting

Jayaraman Maya [1], Katakam Sivaprasad [1,*], Guttula Venkata Sarath Kumar [2], Rustam Baitimerov [3], Pavel Lykov [3] and Konda Gokuldoss Prashanth [4,5,6,*]

[1] Advanced Materials Processing Laboratory, National Institute of Technology Tiruchirappalli, Tiruchirapalli 620015, India; mayajayaraman@gmail.com
[2] Advance Engineering, Ashok Leyland Technical Center, Chennai 600103, India; sarathkumar.gv@gmail.com
[3] Micropowders Technologies Laboratory, Research and Education Center Aerospace Technologies, South Ural State University (SUSU), Lenin Avenue 76, 454080 Chelyabinsk, Russia; rustam_shurmach@mail.ru (R.B.); ooo-sferam-lykov@yandex.ru (P.L.)
[4] Department of Mechanical and Industrial Engineering, Tallinn University of Technology, Ehitajate Tee 5, 19086 Tallinn, Estonia
[5] Erich Schmid Institute of Materials Science, Austrian Academy of Sciences, Jahnstraße 12, A-8700 Leoben, Austria
[6] CBCMT, School of Mechanical Engineering, Vellore Institute of Technology, Vellore 632014, India
* Correspondence: ksp@nitt.edu (K.S.); kgprashanth@gmail.com (K.G.P.)

Abstract: A new class of martensitic stainless steel, namely 06Cr15Ni4CuMo, with applications in marine engineering, was processed by using selective laser melting (SLM). A body-centered cubic martensitic microstructure was observed, and the microstructure was compared with wrought 410 martensitic stainless steel. The SLM-processed sample showed a hardness of 465 ± 10 $HV_{0.5}$, which was nearly 115 $HV_{0.5}$ less than the wrought counterpart. Similarly, the SLM-processed sample showed improved YS and UTS, compared with the wrought sample. However, reduced ductility was observed in the SLM-processed sample due to the presence of high dislocation density in these samples. In addition, 71% volume high-angle grain boundaries were observed, corroborating the high strength of the material. The corrosion behavior was investigated in seawater, and the corrosion resistance was found to be 0.025 mmpy for the SLM-processed 06Cr15Ni4CuMo steel and 0.030 mmpy for wrought 410 alloys, showing better corrosion resistance in the SLM-processed material.

Keywords: selective laser melting (SLM); microstructure; mechanical properties; corrosion

Citation: Maya, J.; Sivaprasad, K.; Sarath Kumar, G.V.; Baitimerov, R.; Lykov, P.; Prashanth, K.G. Microstructure, Mechanical Properties, and Corrosion Behavior of 06Cr15Ni4CuMo Processed by Using Selective Laser Melting. *Metals* **2022**, *12*, 1303. https://doi.org/10.3390/met12081303

Academic Editors: Praveen Sathiyamoorthi and Manogna Karthik Gangaraju

Received: 25 June 2022
Accepted: 2 August 2022
Published: 3 August 2022

Publisher's Note: MDPI stays neutral with regard to jurisdictional claims in published maps and institutional affiliations.

1. Introduction

To meet the high demands in the marine industries for the manufacturing of good-quality parts with reasonable cost and reduced lead times, additive manufacturing (AM) technology is used in many applications, including in the shipbuilding industry [1,2]. Steels are the most used alloy systems in marine industries [3,4]. Even though traditional manufacturing techniques such as casting, machining, powder metallurgy, and welding have been used to produce different types of stainless-steel grades [5–7], AM-based technologies have their applications. AM has been adapted for fabricating components with ultra-complex shapes and is limited in number based on customization [8–11]. AM involves layer-by-layer material deposition to build net-shape complex objects without extensive tooling/die [12]. The potential recycling of the feedstock leads to materials saving [13], making it a green technology. Different AM processes such as electron beam melting (EBM), fused deposition modeling (FDM), wire arc additive manufacturing (WAAM), etc., have been developed in the last decade, also including selective laser melting (SLM)/laser powder bed fusion process (LPBF) [14–16].

SLM/LPBF offers the possibility to fabricate a wide variety of materials directly from metal powder (such as Al-based alloys [17–21], Ti-based alloys [22–25], Ni-based [26–29],

Co-based [30,31], Cu-based [32–35], Ag-based [36], cermets [37–41], bulk metallic glasses [42–44], high-entropy alloys [45–48], quasicrystalline materials [49,50], etc.) with improved properties, and the process has been widely adopted in the industrial sectors [35,51,52]. During the SLM process, the local melting of powders occurs due to the defined laser irradiation resulting in a shallow and narrow melt pool [53]. The shallow and narrow melt pool results in a refined microstructure due to the high cooling rates (10^4 to 10^6 K/s) offered during solidification [33,42,54]. In addition, the solidification rate and the morphology of the microstructure depend on the position/location of the melt pool, and the cooling rate along the melt pool is not constant [33]. Such solidification conditions existing in the melt pool will lead to anisotropy in the microstructure as a function of length scales [55,56]. As a result, the mechanical behavior of SLM alloys tends to be significantly different from that of their traditionally manufactured counterparts [24,36,57]. It is also very important to note that process parameters during the SLM process play vital roles in dictating the microstructure and, in turn, its properties. The energy imparted to the material is a function of laser power, laser scan speed, hatch distance, and layer thickness [58–60]. In addition, the use of the laser in a continuous or pulsed form also affects the fabrication process [41]. Recently, laser modulation has been introduced, based on which people can precisely modulate the laser parameters within a single pulse to finely define their microstructure [37,38]. In addition, powder-bed preheating, preheating through laser, laser prescanning, laser remelting, etc., can significantly influence the fabrication of parts [39–41,61–63].

SLM-processed materials exhibit better corrosion resistance, and their corrosion behavior depends on the crystal planes and grain size [64–67]. Recently, 06Cr15Ni4CuMo marine-grade steel has been developed for marine applications such as compressors, ice breakers, heavy-duty propeller blades, etc. [68–70]. Limited research has been conducted on the fabrication of 06Cr15Ni4CuMo steel using AM. Only Ruslan et al. [71] reported the fabrication of 06Cr15Ni4CuMo steel via direct laser deposition (DLD), where the authors analyzed the mechanical properties of the 06Cr15Ni4CuMo steel after heat treatment. Since there are not many reports that deal with a novel material such as 06Cr15Ni4CuMo steel processed via LPBF/SLM process, and limited literature is available on their microstructure and properties, the present work aimed to explore the microstructure of 06Cr15Ni4CuMo steel fabricated via SLM and to study their properties in as-prepared conditions for marine applications. Detailed microstructural characterization was carried out including grain orientation and texture with electron backscatter diffraction (EBSD) and orientation imaging microscopy (OIM) techniques. In addition, potentiodynamic polarization tests were performed at room temperature in seawater to investigate their corrosion behavior.

2. Materials and Methods

SLM-processed 06Cr15Ni4CuMo and wrought 410 alloys were chosen for this study. The 06Cr15Ni4CuMo powder originates from SeferaM LLC, Chelyabinsk, Russia, and is made according to the Russian standards, namely the GOST 977-88 standard [72]. The morphology of the powder (spherical morphology), the existing phases (martensitic phase), and the EDS (JEOL Ltd., Tokyo, Japan) compositional analysis of the powder are shown in Figure 1. SLM samples (size: diameter—Φ10 mm and length—25 mm) were fabricated with a layer thickness of 25 µm on a selective laser melting device (Realizer SLM 50, Borchen, Germany), using a gas-atomized powder with 33 µm particle size at 96 W laser power, a hatch distance of 120 µm, exposure time of 25 µs, and a point distance of 25 µm (scanning speed: 1000 mm/s). The hatch direction between the layers was maintained the same. The entire process was carried out under a nitrogen atmosphere to avoid possible oxidation during the SLM process. Samples according to ASTM E8 (non-standard) dimensions were used for this study. The chemical composition was evaluated using optical emission spectroscopy (OES) with Spectro (POES, Model No. PMI Master Smart, Serial No. 5770096, Hitachi, Uedem, Germany). The OES chemical composition results are tabulated in Table 1. The density of the samples was measured at ambient conditions using the Archimedes method (ASTM B962). Structural characterization was performed using an X-ray diffraction unit (Rigaku

Ultima IV, Rigaku, Neu-Isenburg, Germany) with Cu–Kα radiation (1.546 Å) operated at 30 mA and 40 kV. All the diffractograms were recorded in the 2θ range: 20° to 140° with a step size of 0.05°at a scanning rate of 1°/min. The lattice strain, average crystallite size, and dislocation density were calculated from the X-ray diffractograms [61–63]. Samples were metallographically polished to obtain a scratch-free surface. The specimens were then chemically etched using 33 mL HCl + 33 mL ethanol + 33 mL water + 1.5 g $CuCl_2$, for 30 s. Scanning electron microscopy (FESEM, Gemini300, ZEISS, Peine, Germany) was applied to observe the microstructural features and corrosion surface.

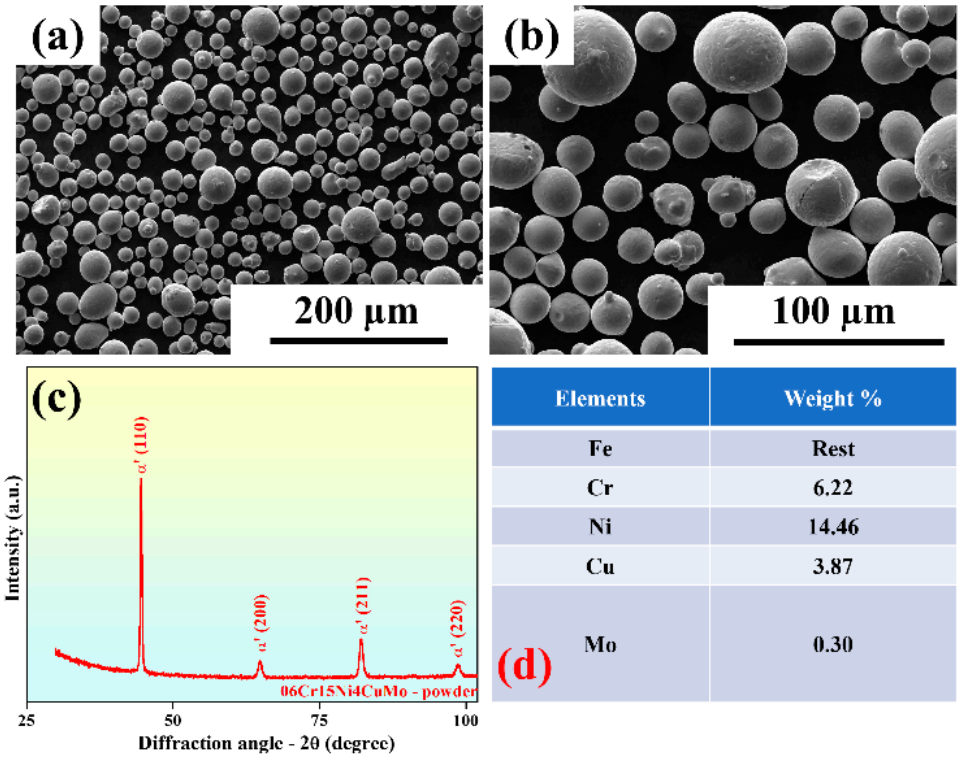

Elements	Weight %
Fe	Rest
Cr	6.22
Ni	14.46
Cu	3.87
Mo	0.30

Figure 1. (**a**,**b**) Scanning electron microscopy images of the 06Cr15Ni4CuMo powder, (**c**) structural characterization by X-ray diffraction, and (**d**) energy-dispersive spectroscopy analysis showing the chemical composition of the powder.

Table 1. Chemical composition (wt.%) of SLM-processed 06Cr15Ni4CuMo and 410 steel.

Alloy	C	Si	Mn	Cr	Mo	Ni	Cu	Fe
06Cr15Ni4CuMo	0.03	0.30	0.87	13.98	0.36	3.97	0.80	Balance
410 steel	0.06	0.61	0.24	12.10	0.24	0.15	0.05	Balance

The specimen was characterized for its grain morphology and orientation by means of an electron back-scattered diffraction (EBSD) technique using an FEI Nova Nano SEM450 instrument (FEI, Stuttgart, Germany) equipped with a TSL OIM data processing software (V8, EDAX, NewYork, NY, USA) system operated at an accelerated voltage of 20 kV, with a step size of 0.5 µm, after electropolishing in a solution of perchloric acid and ethanol (2:8 vol/vol) at a DC voltage of 16 V for 15 s. Vickers microhardness measurements (Hv) were conducted using a Shimadzu digital microhardness tester (Scimadzu, Duisburg, Germany) with a load of 0.5 and a dwell time of 10 s. The microhardness values reported in this manuscript are average values of six test results. Tensile tests were performed on the ASTM E8 miniature samples (along the building direction) using a Tinius Olsen, H25KL testing machine (Tinius Olsen, Surrey, UK) with a strain rate of 5×10^{-3}/s. An ACM Gill AC potentiostat was used to conduct the potentiodynamic polarization test at room

temperature with a three-electrode electrochemical system in seawater with a scan rate of 100 mV/min on an exposed area of 0.5 cm^2 (which was polished according to standards).

3. Results

3.1. Chemical Composition and Density

The chemical compositions of the SLM-processed 06Cr15Ni4CuMo and wrought 410 steel are listed in Table 1. The chemical analysis of these samples showed that the material contained a high amount of Cr (13.98%), leading to a density of 7.6 g/cm^3, which is typical for martensitic steel. The relative density of the SLM-processed 06Cr15Ni4CuMo sample was found to be around 98.5%. On the other hand, the wrought 410 steel had 12.10% Cr, which was nearly 1.88% less than that in the 06Cr15Ni4CuMo steel. However, the compositions were very similar, leading to a single-phased martensitic structure; hence, wrought 410 steel can be taken as a counterpart of SLM-processed 06Cr15Ni4CuMo steel.

3.2. Phase Analysis

The XRD pattern of the sample is shown in Figure 2a. Both the patterns, the SLM as-prepared 06Cr15Ni4CuMo and wrought 410 steel, exhibited the same diffraction peaks corresponding to the martensite phase (α'). Moreover, the patterns suggested that both the samples had only one phase (martensite), and peaks corresponding to any other phase were absent. The lattice strain and crystallite size calculated by the Williamson–Hall peak technique from the X-ray diffraction profile analysis (XRDLPA) are furnished in Table 2. As seen, the crystallite size was found to be 16.55 nm, and the lattice strain was observed to be 0.2065 for the SLM-processed 06Cr15Ni4CuMo martensitic steel. The dislocation density was calculated to be around $5 \times 10^{14}/m^2$, which is one order of magnitude higher than most cast steel products [73–75]. On the other hand, the wrought 410 steel showed an increased crystallite size of 36.55 nm and an increased lattice strain of 0.2031 due to the cold working process involved. Even after such a cold working process, the dislocation density for the 410 steel (9×10^{13} m/m^3) was less than that of the SLM material. This suggests that the extreme cooling rates observed during SLM will have distinct influences on the crystallite size and internal defects of the material. Nevertheless, the internal strain values in the SLM-processed 06Cr15Ni4CuMo and wrought 410 steel were found to be similar. The EDS analysis of the SLM sample in Figure 2b shows no significant difference in the composition of the parts, compared with the EDS composition of the powder furnished in Figure 1d. The EDS results suggested that no foreign particles/phases/contamination were diffused into the parts during the SLM fabrication process.

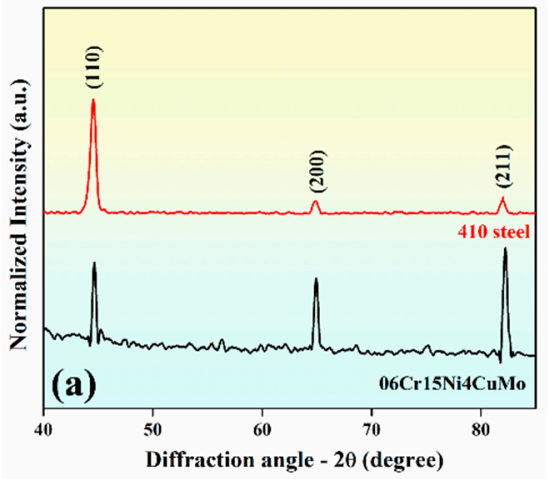

Elements	Weight %
Fe	Rest
Cr	6.41
Ni	15.11
Cu	4.01
Mo	0.28

(b)

Figure 2. (**a**) X-ray diffraction patterns of SLM-processed 06Cr15Ni4CuMo and wrought 410 steel and (**b**) energy-dispersive spectroscopy data of the SLM-processed 06Cr15Ni4CuMo material.

Table 2. Table showing the crystallite size, dislocation density, and lattice strain calculated from the X-ray diffraction line profile analysis for both SLM-processed 06Cr15Ni4CuMo and wrought 410 alloys.

Values	06Cr15Ni4CuMo	410 Steel
Crystallite size	16.55 nm	36.55 nm
Lattice Strain	0.2065	0.2031
Dislocation density	5×10^{14} m/m^3	9×10^{13} m/m^3

3.3. Microstructure

The SEM micrographs of both SLM-processed 06Cr15Ni4CuMo and wrought 410 steel are shown in Figure 3. The SLM-processed 06Cr15Ni4CuMo steel exhibited a single-phase martensitic structure, typical for the SLM process. The rapid quenching of the molten metal, due to localized laser melting during SLM, led to the formation of parallel martensitic laths bundling within a grain. However, no retained austenite was found from the microstructure, corroborating the XRD results. On the other hand, the wrought 410 steel microstructure showed a completely different microstructural morphology. It comprised martensite and some amount of ferrite. The presence of ferrite was absent in the XRD patterns, suggesting that it is present below the deductible limits of the XRD process. Furthermore, 410 steel is a cold-rolled steel product formed under an annealed condition to relieve the internal stresses generated during cold rolling and, hence, showed a distinctly different microstructural morphology from that of the SLM sample.

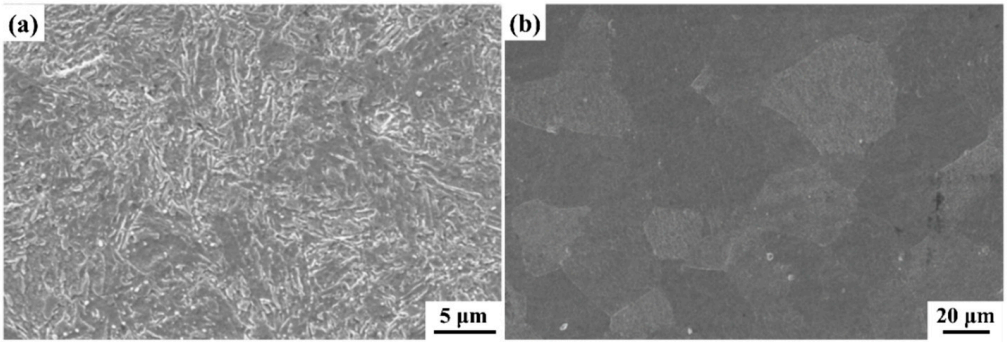

Figure 3. Scanning electron images of (**a**) SLM as-prepared 06Cr15Ni4CuMo steel and (**b**) wrought 410 martensitic stainless steel in annealed condition.

The inverse pole figure maps shown in Figure 4a represent the grain orientation with reference to the crystal lattice for SLM-processed 06Cr15Ni4CuMo, suggesting the presence of a fine-grained microstructure (670 ± 6 nm) with clear grain boundaries (Figure 4e). The grains were preferentially orientated along the (111) direction, suggesting the presence of texture, which can be seen by the blue color dominance in the orientation map. The pole figures shown in Figure 4c confirmed the development of (111) fiber texture, with peak intensities no less than 1.68 times the multiples of uniform density (MUD). The grain boundary map with color gradation obtained with EBSD analysis shown in Figure 4b suggested the presence of a large volume fraction of high-angle grain boundaries and less than 20% volume fraction of low-angle grain boundaries (Figure 4d).

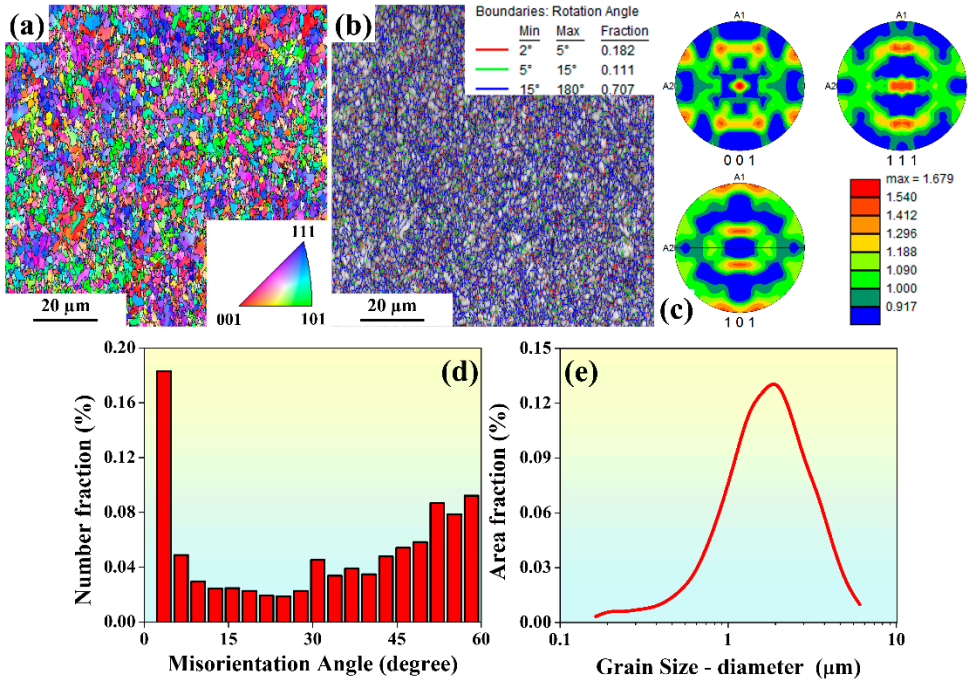

Figure 4. The electron back-scattered diffraction (EBSD) analysis of the SLM-processed 06Cr15Ni4CuMo martensitic steel: (**a**) inverse pole figure (IPF) map; (**b**) grain boundary map; (**c**) pole figures; (**d**) misorientation angle plot; (**e**) grain size distribution plot.

3.4. Mechanical Properties

The mechanical properties of the sample were determined by hardness and room temperature tensile tests. The hardness of the 06Cr15Ni4CuMo steel sample was observed to be 465 ± 10 $HV_{0.5}$, and for wrought 410 stainless steel, the Vickers microhardness was found to be 340 ± 9 $HV_{0.5}$. It can be observed that the SLM-processed 06Cr15Ni4CuMo steel had increased hardness, compared with the wrought counterpart [71], like most SLM-processed samples showing improved properties [30,52,76]. The room-temperature tensile properties of the SLM-processed 06Cr15Ni4CuMo steel showed a yield strength (YS) of 688 MPa, ultimate tensile strength (UTS) of 1137 MPa, and ductility of 28%. The wrought equivalent alloy showed a YS of 230 ± 10 MPa, with 558 ± 20 MPa UTS and 62 ± 5% ductility (as shown in Figure 5). The results demonstrated that the high cooling rates observed during the SLM process led to fine microstructures (fine martensitic laths) and, hence, improved strength, at least twice that of the wrought counterpart. The results are like the results of most SLM-processed materials, namely the fine/unique SLM microstructures lead to improved properties compared with their counterparts produced by conventional methods [57,77–81].

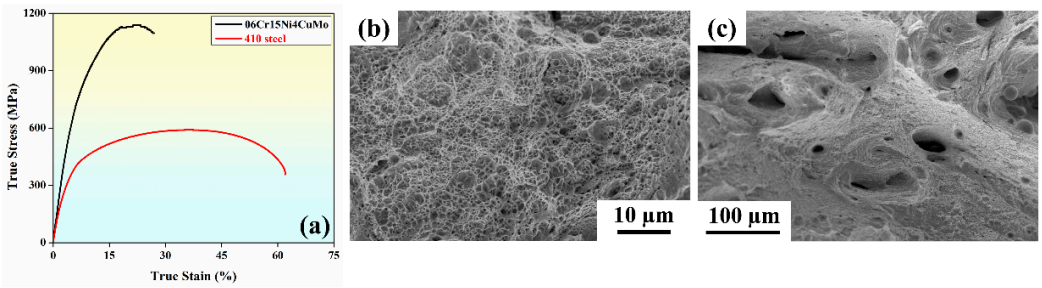

Figure 5. (**a**) True stress–strain curves for the SLM-fabricated 06Cr15Ni4CuMo and wrought 410 martensitic steel samples; (**b**,**c**) fracture surface observed in the SLM-fabricated 06Cr15Ni4CuMo sample.

In addition, DED-processed 06Cr15Ni4CuMo steel showed a hardness value of 340 HV as opposed to the superior hardness of the SLM-processed material (465 HV). However, unlike the hardness results, the tensile properties did not vary significantly between samples produced with DED and SLM [71]. When processed with DED, the 06Cr15Ni4CuMo steel showed a YS of 792 MPa and a UTS of 1088 MPa with 8% ductility, compared with the SLM counterpart, which offered improved UTS (1137 MPa) and ductility (28%) and a marginally reduced YS (688 MPa) [71]. The fracture surface of the SLM-processed sample showed the presence of dimples, corroborating ductility. In addition, pores were observed in these samples (Figure 5b,c), which hampered their ductility and strength. The presence of such defects in the SLM-processed samples led to premature failure in these samples.

In the case of the SLM-processed material, the strength of the alloy increased because of the following factors: (1) a refined microstructure (crystallite size—16.55 nm); (2) the presence of a single martensitic phase; (3) an increased volume of dislocation density (5×10^{14} m/m^3), which was one or two orders of magnitude higher than the values observed for the wrought specimens; and (4) solid solution strengthening [4,14,30,32,82–84]. It is also for the very same reason that the increase in the volume of dislocations (dislocation density) leaves little room for the additional generation of dislocation and dislocation movement during mechanical loading. Since the dislocation movement was severely obstructed, and the generation of new dislocations was restricted, the material had little ductility. It may also be argued in a way that the activation volume for this type of SLM-processed material is $>100 \times 10^3$, thus leading to bulk forest hardening and little plasticity [85–87]. In addition, these additively manufacturing materials tend to fail prematurely due to the presence of both internal and external defects, which also hampers their deformability [36]. Hence, the SLM-processed material showed improved strength at the expense of its plasticity.

3.5. Corrosion Studies

The Tafel curve depicted in Figure 6 was used to assess the corrosion behavior of the SLM-processed 06Cr15Ni4CuMo and wrought 410 steel samples. Several parameters, namely corrosion potential (E_{corr}), corrosion current (I_{corr}), and pitting potential (E_{pit}), were recorded with the help of corrosion analysis software integrated into the ACM Gill AC electrochemical unit. Corrosion comparative studies between 06Cr15Ni4CuMo AM alloy and wrought 410 martensitic stainless steel are tabulated in Table 3. Faraday's law in terms of penetration rate was applied to calculate the corrosion rate and found to be 0.025 mmpy for the SLM-processed 06Cr15Ni4CuMo and 0.030 mmpy for the wrought 410 martensitic stainless steel. The corrosion surface analyzed via SEM showed the presence of localized corrosion pits (Figure 6).

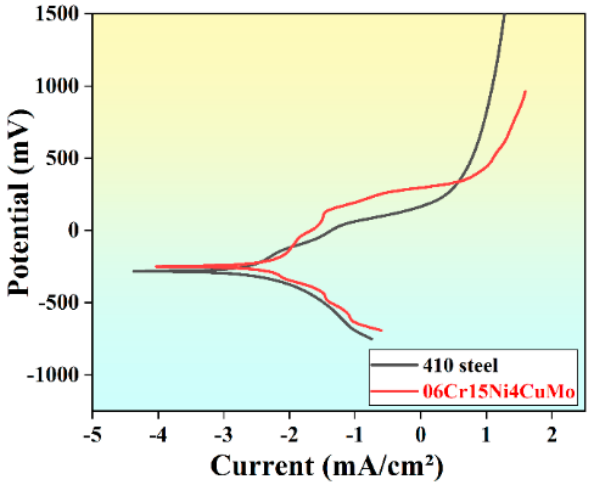

Figure 6. Potentiodynamic polarization curves for the SLM-fabricated 06Cr15Ni4CuMo and wrought 410 martensitic steel samples.

Table 3. Corrosion rate comparison between 06Cr15Ni4CuMo steel and 410 stainless steel.

Values	06Cr15Ni4CuMo Steel (SLM)	410 Steel
E_{Corr} (mV)	−254.2	−267.3
I_{Corr} (mA/cm^2)	−2.31	−2.68
E_{pit}	147.08	48.28
Corrosion rate (mmpy)	0.025	0.030

Localized corrosion attack on the metal surface due to breaking of the passive film and the corrosion pits found were initiated on the sample surface at ~147 V. The largest pit with 75 µm diameter and 409 µm^2 area was observed for the SLM-processed 06Cr15Ni4CuMo. For the wrought 410 steel, corrosion pits were formed at around 48 V, the pit size was measured to be 95 µm, and its equivalent area was found to be 2015 µm^2. The SLM-processed 06Cr15Ni4CuMo sample exhibited better corrosion resistance than the wrought 410 steel due to higher E_{corr} and lower I_{corr} values [88].

4. Discussion

The chemical compositions of both 06Cr15Ni4CuMn and 410 steel revealed a relatively single-phase martensitic microstructure. The morphology of the microstructure observed in these two samples was different due to the differences in their processing conditions. The corrosion behavior in both these materials was rather similar, leading to a localized corrosion attack on the metal surface due to the breaking of the passive film and the observed corrosion pits, which were initiated on the sample's surface at ~147 V and ~48 V, respectively, for SLM-processed 06Cr15Ni4CuMn and wrought 410 steel. The largest pit with 75 µm diameter and 409 µm^2 area was observed for the SLM-processed 06Cr15Ni4CuMo steel, and for wrought 410 steel corrosion, a pit diameter of 95 µm with its equivalent area of 2015 µm^2 was observed. The SLM-processed 06Cr15Ni4CuMo sample exhibited better corrosion resistance than the wrought 410 steel due to higher E_{corr} and lower I_{corr} values [88]. Generally, the presence of Cr in steel imparts corrosion resistance by forming a stable oxide layer, and in these two samples, the Cr content was ~13% for SLM-processed 06Cr15Ni4CuMo and ~12% for wrought 410 martensitic stainless steel, suggesting good corrosion resistance. In addition, the addition of Ni and Mo improved its resistance to attack by NaCl solution. Additionally, a comparison of the chemical composition related to this material can be made with an analog of CA6NM martensitic stainless steel by Ruslan et al. [71].

The lath martensite formed is of body-centered cubic phase (BCC) unlike the body-centered tetragonal (BCT) phase observed for the conventional lath martensite. This is due to its lower carbon content and lack of lattice distortion. The SLM process, which is associated with repeated heating and cooling cycles due to frequent reheating and remelting of subsequent layers [89], leads to a certain degree of internal strain but not adequate lattice distortion to form BCT martensite. The mechanical properties are strongly dependent on the microstructure, and the SLM sample undergoes in situ tempering due to repeated heating and cooling cycles. During the process, the first layer is solidified, and when the second layer is formed, due to conduction, the previous layer is heated, resulting in tempering. Similarly, the second layer is also tempered when the third layer is formed, and this process continues [90,91]. The observed α′ microstructure is like the one reported by Mirakboli et al. [70], in which the low carbon martensite was obtained during SLM, and the XRD pattern strengthens the argument of the likely formation of low-carbon martensite during the laser melting of martensitic stainless steel [92].

Any grain boundaries having a misorientation angle between 2° and 15° are known as low-angle grain boundaries (LAGBs). Low-angle grain boundaries result in the formation of martensitic laths, which separate dislocation forests and low-density dislocations. They act as stopping points for dislocation movements, and they become sessile at these points. Any misorientation angles greater than 15° are known as high-angle grain boundaries (HAGBs), denoted in green and blue lines, respectively, on the map. A volume of 71%

HAGB and only less than 20% LAGB were observed (Figure 4). The HAGB distributed the plastic strain evenly through the material, resulting in superior strength. Additionally, in high-angle misorientation, the number of active slip systems decreased, resulting in the slower movement of dislocations and reduction in plastic deformation, and finally increased strength [93]. The texture of the fabricated samples depends on the temperature, temperature gradient (G), and the cooling rate (R) observed during the SLM process [94]. Fine martensitic crystals were formed due to higher cooling rates, and the obtained crystallographic structures were oriented in the (110) <111> direction, which is in line with the observations of Khodabakshi et al. [95], in a study in which the crystallographic planes of 410 stainless steel were oriented in similar directions. The martensite formed due to a higher cooling rate corroborated the higher hardness observed for the SLM-fabricated steel sample. Along with higher cooling rates, the concentration of alloying elements such as Cr, Ni, and Mo increases the hardenability, and this also contributes to higher hardness values [96]. Higher YS and UTS values were observed because of the presence of lath martensite in the microstructure and due to the presence of a larger amount (71%) of HAGB. The higher the volume of HAGB, the more the grain boundary areas, which, in turn, impede the dislocation movement, finally resulting in an increase in the strength of the material [97].

The thermodynamic tendency of forming a passivation layer was higher for the 410 steel samples, as E_{Corr} shifted toward a more cathodic (−267.34 mV) potential than that of the SLM sample (−254.22 mV). The rate of corrosion was also higher in wrought 410 stainless steel than in the SLM-fabricated 06Cr15Ni4CuMn sample, which can be explained by the E_{corr} value. In general, pitting potential is the point at which pitting corrosion starts and below which the pits will not initiate. The SLM sample exhibited 3 times higher pitting potential than the 410 stainless steel sample, indicating higher resistance to pitting corrosion in the SLM sample than in the 410 steel counterparts. This could be attributed to the stable passive layer formed on its surface. Heavy alloying elements such as Cr, Ni, Cu, and Mo in SLM alloys may form complex passive oxide layers, which, in turn, protect the bulk material. Moreover, the SLM process, because of its melting route, may enable the formation of a more complex oxide passive layer on the material's surface than on the wrought 410 stainless steel. Until the stable passive layer protects the bulk material, pitting resistance can be maintained, and it is conveyed by passivation potential, below which the metal/alloy retains its passivity. Above the passivation potential, pits do not propagate, thus providing pitting resistance by protecting the bulk material [98,99]. As observed in Figure 7, the size of the pits was higher for 410 steel, and this is due to having lower pitting corrosion resistance than the SLM-processed 06Cr15Ni4CuMo alloy. Pitting resistance depends on the Cr% and the alloy with elements such as Ni and Mo. Since 06Cr15Ni4CuMo has higher alloy content than wrought 410 martensitic stainless steel, it has higher pitting resistance [100,101].

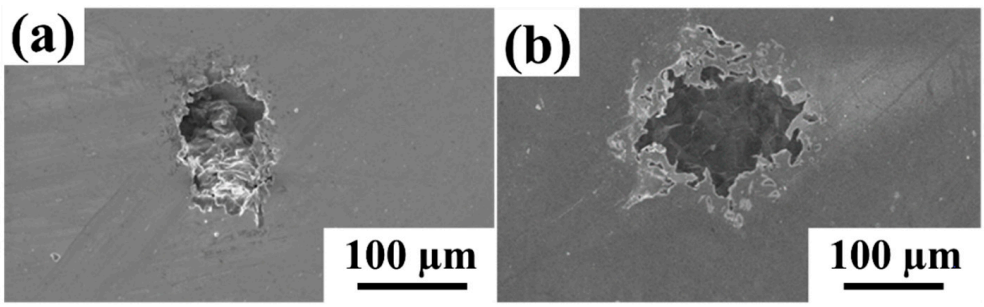

Figure 7. The scanning electron microscopy images of the (**a**) SLM-processed 06Cr15Ni4CuMo (**b**) wrought 410 stainless steel show the presence of localized corrosion pits.

5. Conclusions

In this study, the 06Cr15Ni4CuMo alloy was successfully processed using SLM. The 06Cr15Ni4CuMo alloy showed a presence of BCC martensite microstructure. For comparison, wrought 410 martensitic stainless steel was employed, which also showed a BCC martensitic structure, similar to the 06Cr15Ni4CuMo alloy. Due to the high cooling rates observed during the SLM process, the SLM-processed 06Cr15Ni4CuMo showed improved hardness, YS, and UTS over the wrought 410 steel but at the expense of ductility. The potentiodynamic polarization curves confirmed better corrosion resistance in the SLM-processed martensitic stainless steel than in the wrought 410 martensitic stainless steel. Corrosion rates were observed to be 0.025 mmpy and 0.030 mmpy for the SLM-processed 06Cr15Ni4CuMo and wrought 410 martensitic stainless steel, respectively. The tendency for pitting was higher in the wrought 410 martensitic stainless steel than in the SLM-processed stainless steel. These results suggest that the 06Cr15Ni4CuMo alloy fabricated via SLM can be successfully employed for parts in marine applications.

Author Contributions: Conceptualization, K.S. and K.G.P.; methodology, J.M.; validation, J.M., K.S. and K.G.P.; formal analysis, J.M., G.V.S.K., R.B. and P.L.; investigation, J.M., G.V.S.K., R.B. and P.L.; resources, K.S., P.L. and K.G.P.; writing—original draft preparation, J.M. and G.V.S.K.; writing—review and editing, R.B., K.S. and K.G.P.; supervision, K.S. and K.G.P.; project administration, K.S. and K.G.P.; funding acquisition, K.S. and K.G.P. All authors have read and agreed to the published version of the manuscript.

Funding: Authors would also thank the SPARC program (SPARC/2018-2019/P361/SL) from the Ministry of Human Resources and Development (MHRD), Government of India, for the financial support. Funding from the European Regional Development Grant (ASTRA 6-6) is greatly acknowledged. Further financial support from the High-End Foreign Experts Recruitment Program (G2021163004L) and the Guangdong International Science and Technology Cooperation Program (2021A0505050002) are appreciated.

Institutional Review Board Statement: Not applicable.

Informed Consent Statement: Not applicable.

Data Availability Statement: Data may be shared by authors upon reasonable request.

Conflicts of Interest: The authors declare no conflict of interest.

References

1. Prashanth, K.G. Selective Laser Melting: Materials and Applications. *J. Manuf. Mater. Process.* **2020**, *4*, 13. [CrossRef]
2. DebRoy, T.; Wei, H.L.; Zuback, J.S.; Mukherjee, T.; Elmer, J.W.; Milewski, J.O.; Beese, A.M.; Wilson-Heid, A.; De, A.; Zhang, W. Additive Manufacturing of Metallic Components—Process, Structure and Properties. *Prog. Mater. Sci.* **2018**, *92*, 112–224. [CrossRef]
3. Oh, S.J.; Cook, D.C.; Townsend, H.E. Atmospheric Corrosion of Different Steels in Marine, Rural and Industrial Environments. *Corros. Sci.* **1999**, *41*, 1687–1702. [CrossRef]
4. Kumar, D.; Shankar, G.; Prashanth, K.G.; Suwas, S. Texture Dependent Strain Hardening in Additively Manufactured Stainless Steel 316L. *Mater. Sci. Eng. A* **2021**, *820*, 141483. [CrossRef]
5. Khodabakhshi, F.; Farshidianfar, M.H.; Gerlich, A.P.; Nosko, M.; Trembošová, V.; Khajepour, A. Microstructure, Strain-Rate Sensitivity, Work Hardening, and Fracture Behavior of Laser Additive Manufactured Austenitic and Martensitic Stainless Steel Structures. *Mater. Sci. Eng. A* **2019**, *756*, 545–561. [CrossRef]
6. Promakhov, V.; Zhukov, A.; Ziatdinov, M.; Zhukov, I.; Schulz, N.; Kovalchuk, S.; Dubkova, Y.; Korsmik, R.; Klimova-Korsmik, O.; Turichin, G.; et al. Inconel 625/TiB2 Metal Matrix Composites by Direct Laser Deposition. *Metals* **2019**, *9*, 141. [CrossRef]
7. Balcı, Ö.; Prashanth, K.G.; Scudino, S.; Somer, M.; Eckert, J. Powder Metallurgy of Al-Based Composites Reinforced with Fe-Based Glassy Particles: Effect of Microstructural Modification. *Part. Sci. Technol.* **2019**, *37*, 286–291. [CrossRef]
8. Prashanth, K.; Löber, L.; Klauss, H.-J.; Kühn, U.; Eckert, J. Characterization of 316L Steel Cellular Dodecahedron Structures Produced by Selective Laser Melting. *Technologies* **2016**, *4*, 34. [CrossRef]
9. Attar, H.; Löber, L.; Funk, A.; Calin, M.; Zhang, L.C.; Prashanth, K.G.; Scudino, S.; Zhang, Y.S.; Eckert, J. Mechanical Behavior of Porous Commercially Pure Ti and Ti-TiB Composite Materials Manufactured by Selective Laser Melting. *Mater. Sci. Eng. A* **2015**, *625*, 350–356. [CrossRef]

10. Hameed, P.; Liu, C.F.; Ummethala, R.; Singh, N.; Huang, H.H.; Manivasagam, G.; Prashanth, K.G. Biomorphic Porous Ti6Al4V Gyroid Scaffolds for Bone Implant Applications Fabricated by Selective Laser Melting. *Prog. Addit. Manuf.* **2021**, *6*, 455–469. [CrossRef]
11. Raheem, A.A.; Hameed, P.; Whenish, R.; Elsen, R.S.; Aswin, G.; Jaiswal, A.K.; Prashanth, K.G.; Manivasagam, G. A Review on Development of Bio-Inspired Implants Using 3d Printing. *Biomimetics* **2021**, *6*, 65. [CrossRef] [PubMed]
12. Frazier, W.E. Metal Additive Manufacturing: A Review. *J. Mater. Eng. Perform.* **2014**, *23*, 1917–1928. [CrossRef]
13. Alam, M.K.; Mehdi, M.; Urbanic, R.J.; Edrisy, A. Electron Backscatter Diffraction (EBSD) Analysis of Laser-Cladded AISI 420 Martensitic Stainless Steel. *Mater. Charact.* **2020**, *161*, 110138. [CrossRef]
14. Kumar, D.; Jhavar, S.; Arya, A.; Prashanth, K.G.; Suwas, S. Mechanisms Controlling Fracture Toughness of Additively Manufactured Stainless Steel 316L. *Int. J. Fract.* **2021**, *235*, 61–78. [CrossRef]
15. Singh, S.; Jinoop, A.N.; Palani, I.A.; Paul, C.P.; Tomar, K.P.; Prashanth, K.G. Microstructure and Mechanical Properties of NiTi-SS Bimetallic Structures Built Using Wire Arc Additive Manufacturing. *Mater. Lett.* **2021**, *303*, 130499. [CrossRef]
16. Singh, S.; Jinoop, A.N.; Kumar, G.T.A.V.T.; Shukla, A.; Palani, I.A.; Resnina, N.; Paul, C.P.; Prashanth, K.G. Laser Hybrid Wire Arc Additive Manufacturing for Fabricating Thin Sections. *Trans. Indian Natl. Acad. Eng.* **2021**, *7*, 175–183. [CrossRef]
17. Olakanmi, E.O.; Cochrane, R.F.; Dalgarno, K.W. A Review on Selective Laser Sintering/Melting (SLS/SLM) of Aluminium Alloy Powders: Processing, Microstructure, and Properties. *Prog. Mater. Sci.* **2015**, *74*, 401–477. [CrossRef]
18. Aboulkhair, N.T.; Simonelli, M.; Parry, L.; Ashcroft, I.; Tuck, C.; Hague, R. 3D Printing of Aluminium Alloys: Additive Manufacturing of Aluminium Alloys Using Selective Laser Melting. *Prog. Mater. Sci.* **2019**, *106*, 100578. [CrossRef]
19. Wang, Z.; Scudino, S.; Eckert, J.; Prashanth, K.G. Selective Laser Melting of Nanostructured Al-Y-Ni-Co Alloy. *Manuf. Lett.* **2020**, *25*, 21–25. [CrossRef]
20. Wang, P.; Li, H.C.; Prashanth, K.G.; Eckert, J.; Scudino, S. Selective Laser Melting of Al-Zn-Mg-Cu: Heat Treatment, Microstructure and Mechanical Properties. *J. Alloys Compd.* **2017**, *707*, 287–290. [CrossRef]
21. Wang, P.; Yu, S.; Shergill, J.; Chaubey, A.; Eckert, J.; Prashanth, K.G.; Scudino, S. Selective Laser Melting of Al-7Si-0.5Mg-0.5Cu: Effect of Heat Treatment on Microstructure Evolution, Mechanical Properties and Wear Resistance. *Acta Metall. Sin.* **2021**, *1*, 389–396. [CrossRef]
22. Qin, P.T.; Damodaram, R.; Maity, T.; Zhang, W.W.; Yang, C.; Wang, Z.; Prashanth, K.G. Friction Welding of Electron Beam Melted Ti-6Al-4V. *Mater. Sci. Eng. A* **2019**, *761*, 138045. [CrossRef]
23. Ehtemam-Haghighi, S.; Prashanth, K.G.; Attar, H.; Chaubey, A.K.; Cao, G.H.; Zhang, L.C. Evaluation of Mechanical and Wear Properties of Ti-XNb-7Fe Alloys Designed for Biomedical Applications. *Mater. Des.* **2016**, *111*, 592–599. [CrossRef]
24. Agius, D.; Kourousis, K.I.; Wallbrink, C. A Review of the As-Built SLM Ti-6Al-4V Mechanical Properties towards Achieving Fatigue Resistant Designs. *Metals* **2018**, *8*, 75. [CrossRef]
25. Gorsse, S.; Hutchinson, C.; Gouné, M.; Banerjee, R. Additive Manufacturing of Metals: A Brief Review of the Characteristic Microstructures and Properties of Steels, Ti-6Al-4V and High-Entropy Alloys. *Sci. Technol. Adv. Mater.* **2017**, *18*, 584–610. [CrossRef] [PubMed]
26. Lu, Y.; Wu, S.; Gan, Y.; Huang, T.; Yang, C.; Lin, J.; Lin, J. Study on the Microstructure, Mechanical Property and Residual Stress of SLM Inconel-718 Alloy Manufactured by Differing Island Scanning Strategy. *Opt. Laser Technol.* **2015**, *75*, 197–206. [CrossRef]
27. Onuike, B.; Bandyopadhyay, A. Additive Manufacturing of Inconel 718—Ti6Al4V Bimetallic Structures. *Addit. Manuf.* **2018**, *22*, 844–851. [CrossRef]
28. Amato, K.N.; Gaytan, S.M.; Murr, L.E.; Martinez, E.; Shindo, P.W.; Hernandez, J.; Collins, S.; Medina, F. Microstructures and Mechanical Behavior of Inconel 718 Fabricated by Selective Laser Melting. *Acta Mater.* **2012**, *60*, 2229–2239. [CrossRef]
29. Herzog, D.; Seyda, V.; Wycisk, E.; Emmelmann, C. Additive Manufacturing of Metals. *Acta Mater.* **2016**, *117*, 371–392. [CrossRef]
30. Wang, Z.; Tang, S.Y.; Scudino, S.; Ivanov, Y.P.; Qu, R.T.; Wang, D.; Yang, C.; Zhang, W.W.; Greer, A.L.; Eckert, J.; et al. Additive Manufacturing of a Martensitic Co–Cr–Mo Alloy: Towards Circumventing the Strength–Ductility Trade-Off. *Addit. Manuf.* **2021**, *37*, 101725. [CrossRef]
31. Lu, Y.; Wu, S.; Gan, Y.; Zhang, S.; Guo, S.; Lin, J.; Lin, J. Microstructure, Mechanical Property and Metal Release of As-SLM CoCrW Alloy under Different Solution Treatment Conditions. *J. Mech. Behav. Biomed. Mater.* **2016**, *55*, 179–190. [CrossRef] [PubMed]
32. Zhao, C.; Wang, Z.; Li, D.; Kollo, L.; Luo, Z.; Zhang, W.; Prashanth, K.G. Selective Laser Melting of Cu–Ni–Sn: A Comprehensive Study on the Microstructure, Mechanical Properties, and Deformation Behavior. *Int. J. Plast.* **2021**, *138*, 102926. [CrossRef]
33. Zhao, C.; Wang, Z.; Li, D.; Kollo, L.; Luo, Z.; Zhang, W.; Prashanth, K.G. Cu-Ni-Sn Alloy Fabricated by Melt Spinning and Selective Laser Melting: A Comparative Study on the Microstructure and Formation Kinetics. *J. Mater. Res. Technol.* **2020**, *9*, 13097–13105. [CrossRef]
34. Zhao, C.; Wang, Z.; Li, D.; Xie, M.; Kollo, L.; Luo, Z.; Zhang, W.; Prashanth, K.G. Comparison of Additively Manufacturing Samples Fabricated from Pre-Alloyed and Mechanically Mixed Powders. *J. Alloys Compd.* **2020**, *830*, 154603. [CrossRef]
35. Scudino, S.; Unterdörfer, C.; Prashanth, K.G.; Attar, H.; Ellendt, N.; Uhlenwinkel, V.; Eckert, J. Additive Manufacturing of Cu-10Sn Bronze. *Mater. Lett.* **2015**, *156*, 202–204. [CrossRef]
36. Wang, Z.; Xie, M.; Li, Y.; Zhang, W.; Yang, C.; Kollo, L.; Eckert, J.; Prashanth, K.G. Premature Failure of an Additively Manufactured Material. *NPG Asia Mater.* **2020**, *12*, 30. [CrossRef]
37. Maurya, H.S.; Juhani, K.; Sergejev, F.; Prashanth, K.G. Additive Manufacturing of TiC-Based Cermet with Stainless Steel as a Binder Material. *Mater. Today Proc.* **2022**, *57*, 824–828. [CrossRef]

38. Maurya, H.S.; Kosiba, K.; Juhani, K.; Sergejev, F.; Prashanth, K.G. Effect of Powder Bed Preheating on the Crack Formation and Microstructure in Ceramic Matrix Composites Fabricated by Laser Powder-Bed Fusion Process. *Addit. Manuf.* **2022**, *58*, 103013. [CrossRef]
39. Maurya, H.S.; Kollo, L.; Juhani, K.; Sergejev, F.; Prashanth, K.G. Effect of Preheating and Cooling of the Powder Bed by Laser Pulse Shaping on the Microstructure of the TiC Based Cermets. *Ceram. Int.* **2022**, *48*, 20612–20618. [CrossRef]
40. Maurya, H.S.; Kollo, L.; Tarraste, M.; Juhani, K.; Sergejev, F.; Gokuldoss Prashanth, K. Effect of the Laser Processing Parameters on the Selective Laser Melting of TiC-Fe-Based Cermets. *J. Manuf. Mater. Process.* **2022**, *6*, 35. [CrossRef]
41. Maurya, H.S.; Kollo, L.; Tarraste, M.; Juhani, K.; Sergejev, F.; Prashanth, K.G. Selective Laser Melting of TiC-Fe via Laser Pulse Shaping: Microstructure and Mechanical Properties. *3D Print. Addit. Manuf.* **2021**. [CrossRef]
42. Jung, H.Y.; Choi, S.J.; Prashanth, K.G.; Stoica, M.; Scudino, S.; Yi, S.; Kühn, U.; Kim, D.H.; Kim, K.B.; Eckert, J. Fabrication of Fe-Based Bulk Metallic Glass by Selective Laser Melting: A Parameter Study. *Mater. Des.* **2015**, *86*, 703–708. [CrossRef]
43. Zhang, C.; Ouyang, D.; Pauly, S.; Liu, L. 3D Printing of Bulk Metallic Glasses. *Mater. Sci. Eng. R Rep.* **2021**, *145*, 100625. [CrossRef]
44. Pauly, S.; Löber, L.; Petters, R.; Stoica, M.; Scudino, S.; Kühn, U.; Eckert, J. Processing Metallic Glasses by Selective Laser Melting. *Mater. Today* **2013**, *16*, 37–41. [CrossRef]
45. Karimi, J.; Ma, P.; Jia, Y.D.; Prashanth, K.G. Linear Patterning of High Entropy Alloy by Additive Manufacturing. *Manuf. Lett.* **2020**, *24*, 9–13. [CrossRef]
46. Chen, H.; Lu, T.; Wang, Y.; Liu, Y.; Shi, T.; Prashanth, K.G.; Kosiba, K. Laser Additive Manufacturing of Nano-TiC Particles Reinforced CoCrFeMnNi High-Entropy Alloy Matrix Composites with High Strength and Ductility. *Mater. Sci. Eng. A* **2021**, *833*, 142512. [CrossRef]
47. Brif, Y.; Thomas, M.; Todd, I. The Use of High-Entropy Alloys in Additive Manufacturing. *Scr. Mater.* **2015**, *99*, 93–96. [CrossRef]
48. Ostovari Moghaddam, A.; Shaburova, N.A.; Samodurova, M.N.; Abdollahzadeh, A.; Trofimov, E.A. Additive Manufacturing of High Entropy Alloys: A Practical Review. *J. Mater. Sci. Technol.* **2021**, *77*, 131–162. [CrossRef]
49. Prashanth, K.G.; Scudino, S. Quasicrystalline Composites by Additive Manufacturing. *Key Eng. Mater.* **2019**, *818*, 72–76. [CrossRef]
50. Kang, N.; El Mansori, M.; Lin, X.; Guittonneau, F.; Liao, H.L.; Huang, W.D.; Coddet, C. In-Situ Synthesis of Aluminum/Nano-Quasicrystalline Al-Fe-Cr Composite by Using Selective Laser Melting. *Compos. Part B Eng.* **2018**, *155*, 382–390. [CrossRef]
51. Prashanth, K.G.; Scudino, S.; Klauss, H.J.; Surreddi, K.B.; Löber, L.; Wang, Z.; Chaubey, A.K.; Kühn, U.; Eckert, J. Microstructure and Mechanical Properties of Al-12Si Produced by Selective Laser Melting: Effect of Heat Treatment. *Mater. Sci. Eng. A* **2014**, *590*, 153–160. [CrossRef]
52. Prashanth, K.; Scudino, S.; Chatterjee, R.; Salman, O.; Eckert, J. Additive Manufacturing: Reproducibility of Metallic Parts. *Technologies* **2017**, *5*, 8. [CrossRef]
53. Prashanth, K.G.; Eckert, J. Formation of Metastable Cellular Microstructures in Selective Laser Melted Alloys. *J. Alloys Compd.* **2017**, *707*, 27–34. [CrossRef]
54. Singh, S.; Sharma, V.S.; Sachdeva, A. Progress in Selective Laser Sintering Using Metallic Powders: A Review. *Mater. Sci. Technol.* **2016**, *32*, 760–772. [CrossRef]
55. Maity, T.; Chawake, N.; Kim, J.T.; Eckert, J.; Prashanth, K.G. Anisotropy in Local Microstructure—Does It Affect the Tensile Properties of the SLM Samples? *Manuf. Lett.* **2018**, *15*, 33–37. [CrossRef]
56. Zhu, Y.; Tian, X.; Li, J.; Wang, H. The Anisotropy of Laser Melting Deposition Additive Manufacturing Ti-6.5Al-3.5Mo-1.5Zr-0.3Si Titanium Alloy. *Mater. Des.* **2015**, *67*, 538–542. [CrossRef]
57. Suryawanshi, J.; Prashanth, K.G.; Ramamurty, U. Mechanical Behavior of Selective Laser Melted 316L Stainless Steel. *Mater. Sci. Eng. A* **2017**, *696*, 113–121. [CrossRef]
58. Prashanth, K.G.; Scudino, S.; Maity, T.; Das, J.; Eckert, J. Is the Energy Density a Reliable Parameter for Materials Synthesis by Selective Laser Melting? *Mater. Res. Lett.* **2017**, *5*, 386–390. [CrossRef]
59. Scipioni Bertoli, U.; Wolfer, A.J.; Matthews, M.J.; Delplanque, J.P.R.; Schoenung, J.M. On the Limitations of Volumetric Energy Density as a Design Parameter for Selective Laser Melting. *Mater. Des.* **2017**, *113*, 331–340. [CrossRef]
60. Ghayoor, M.; Lee, K.; He, Y.; Chang, C.-H.; Paul, B.K.; Pasebani, S. Selective Laser Melting of 304L Stainless Steel: Role of Volumetric Energy Density on the Microstructure, Texture and Mechanical Properties. *Addit. Manuf.* **2020**, *32*, 101011. [CrossRef]
61. Karimi, J.; Xie, M.S.; Wang, Z.; Prashanth, K.G. Influence of Substructures on the Selective Laser Melted Ti-6Al-4V Alloy as a Function of Laser Re-Melting. *J. Manuf. Process.* **2021**, *68*, 1387–1394. [CrossRef]
62. Karimi, J.; Suryanarayana, C.; Okulov, I.; Prashanth, K.G. Selective Laser Melting of Ti6Al4V: Effect of Laser Re-Melting. *Mater. Sci. Eng. A* **2020**, *805*, 140558. [CrossRef]
63. Karimi, J.; Antonov, M.; Kollo, L.; Prashanth, K.G. Role of Laser Remelting and Heat Treatment in Mechanical and Tribological Properties of Selective Laser Melted Ti6Al4V Alloy. *J. Alloys Compd.* **2022**, *897*, 163207. [CrossRef]
64. Ko, G.; Kim, W.; Kwon, K.; Lee, T.K. The Corrosion of Stainless Steel Made by Additive Manufacturing: A Review. *Metals* **2021**, *11*, 516. [CrossRef]
65. Schindelholz, E.J.; Melia, M.A.; Rodelas, J.M. Corrosion of Additively Manufactured Stainless Steels—Process, Structure, Performance: A Review. *Corrosion* **2021**, *77*, 484–503. [CrossRef]
66. Vignal, V.; Voltz, C.; Thiébaut, S.; Demésy, M.; Heintz, O.; Guerraz, S. Pitting Corrosion of Type 316L Stainless Steel Elaborated by the Selective Laser Melting Method: Influence of Microstructure. *J. Mater. Eng. Perform.* **2021**, *30*, 5050–5058. [CrossRef]
67. Kong, D.; Dong, C.; Ni, X.; Li, X. Corrosion of Metallic Materials Fabricated by Selective Laser Melting. *NPJ Mater. Degrad.* **2019**, *3*, 34. [CrossRef]

68. Winck, L.B.; Ferreira, J.L.A.; Araujo, J.A.; Manfrinato, M.D.; da Silva, C.R.M. Surface Nitriding Influence on the Fatigue Life Behavior of ASTM A743 Steel Type CA6NM. *Surf. Coat. Technol.* **2013**, *232*, 844–850. [CrossRef]
69. Wen, P.; Cai, Z.; Feng, Z.; Wang, G. Microstructure and Mechanical Properties of Hot Wire Laser Clad Layers for Repairing Precipitation Hardening Martensitic Stainless Steel. *Opt. Laser Technol.* **2015**, *75*, 207–213. [CrossRef]
70. Mirakhorli, F.; Cao, X.; Pham, X.T.; Wanjara, P.; Fihey, J.L. Phase Structures and Morphologies of Tempered CA6NM Stainless Steel Welded by Hybrid Laser-Arc Process. *Mater. Charact.* **2017**, *123*, 264–274. [CrossRef]
71. Mendagaliev, R.; Klimova-Korsmik, O.; Promakhov, V.; Schulz, N.; Zhukov, A.; Klimenko, V.; Olisov, A. Heat Treatment of Corrosion Resistant Steel for Water Propellers Fabricated by Direct Laser Deposition. *Materials* **2020**, *13*, 2738. [CrossRef] [PubMed]
72. *GOST 977-88*; Steel Castings—General Technical Specifications. Standards Publishers: Moscow, Russia, 2004.
73. Bertsch, K.M.; Meric de Bellefon, G.; Kuehl, B.; Thoma, D.J. Origin of Dislocation Structures in an Additively Manufactured Austenitic Stainless Steel 316L. *Acta Mater.* **2020**, *199*, 19–33. [CrossRef]
74. Röttger, A.; Boes, J.; Theisen, W.; Thiele, M.; Esen, C.; Edelmann, A.; Hellmann, R. Microstructure and Mechanical Properties of 316L Austenitic Stainless Steel Processed by Different SLM Devices. *Int. J. Adv. Manuf. Technol.* **2020**, *108*, 769–783. [CrossRef]
75. Sprouster, D.J.; Streit Cunningham, W.; Halada, G.P.; Yan, H.; Pattammattel, A.; Huang, X.; Olds, D.; Tilton, M.; Chu, Y.S.; Dooryhee, E.; et al. Dislocation Microstructure and Its Influence on Corrosion Behavior in Laser Additively Manufactured 316L Stainless Steel. *Addit. Manuf.* **2021**, *47*, 102263. [CrossRef]
76. Prashanth, K.G.; Damodaram, R.; Scudino, S.; Wang, Z.; Prasad Rao, K.; Eckert, J. Friction Welding of Al-12Si Parts Produced by Selective Laser Melting. *Mater. Des.* **2014**, *57*, 632–637. [CrossRef]
77. Suryawanshi, J.; Prashanth, K.G.; Ramamurty, U. Tensile, Fracture, and Fatigue Crack Growth Properties of a 3D Printed Maraging Steel through Selective Laser Melting. *J. Alloys Compd.* **2017**, *725*, 355–364. [CrossRef]
78. Suryawanshi, J.; Prashanth, K.G.; Scudino, S.; Eckert, J.; Prakash, O.; Ramamurty, U. Simultaneous Enhancements of Strength and Toughness in an Al-12Si Alloy Synthesized Using Selective Laser Melting. *Acta Mater.* **2016**, *115*, 285–294. [CrossRef]
79. Prashanth, K.G.; Scudino, S.; Eckert, J. Defining the Tensile Properties of Al-12Si Parts Produced by Selective Laser Melting. *Acta Mater.* **2017**, *126*, 25–35. [CrossRef]
80. Tang, S.; Ummethala, R.; Suryanarayana, C.; Eckert, J.; Prashanth, K.G.; Wang, Z. Additive Manufacturing of Aluminum-Based Metal Matrix Composites—A Review. *Adv. Eng. Mater.* **2021**, *23*, 2100053. [CrossRef]
81. Wang, P.; Eckert, J.; Prashanth, K.G.; Wu, M.-W.; Kaban, I.; Xi, L.; Scudino, S. A Review of Particulate-Reinforced Aluminum Matrix Composites Fabricated by Selective Laser Melting. *Trans. Nonferrous Met. Soc. China* **2020**, *30*, 2001–2034. [CrossRef]
82. Sokkalingam, R.; Sivaprasad, K.; Singh, N.; Muthupandi, V.; Ma, P.; Jia, Y.D.; Prashanth, K.G. Subtle Change in the Work Hardening Behavior of Fcc Materials Processed by Selective Laser Melting. *Prog. Addit. Manuf.* **2022**, *7*, 453–461. [CrossRef]
83. Xi, L.; Feng, L.; Gu, D.; Wang, R.; Sarac, B.; Prashanth, K.G.; Eckert, J. ZrC + TiC Synergically Reinforced Metal Matrix Composites with Micro/Nanoscale Reinforcements Prepared by Laser Powder Bed Fusion. *J. Mater. Res. Technol.* **2022**, *19*, 4645–4657. [CrossRef]
84. Xi, L.; Ding, K.; Gu, D.; Guo, S.; Cao, M.; Zhuang, J.; Lin, K.; Okulov, I.; Sarac, B.; Eckert, J.; et al. Interfacial Structure and Wear Properties of Selective Laser Melted Ti/(TiC + TiN) Composites with High Content of Reinforcements. *J. Alloys Compd.* **2021**, *870*, 159436. [CrossRef]
85. Zhu, T.; Li, J.; Samanta, A.; Kim, H.G.; Suresh, S. Interfacial Plasticity Governs Strain Rate Sensitivity and Ductility in Nanostructured Metals. *Proc. Natl. Acad. Sci. USA* **2007**, *104*, 3031–3036. [CrossRef] [PubMed]
86. Wei, Q.; Cheng, S.; Ramesh, K.T.; Ma, E. Effect of Nanocrystalline and Ultrafine Grain Sizes on the Strain Rate Sensitivity and Activation Volume: Fcc versus Bcc Metals. *Mater. Sci. Eng. A* **2004**, *381*, 71–79. [CrossRef]
87. Maity, T.; Prashanth, K.G.; Balçi, Ö.; Wang, Z.; Jia, Y.D.; Eckert, J. Plastic Deformation Mechanisms in Severely Strained Eutectic High Entropy Composites Explained via Strain Rate Sensitivity and Activation Volume. *Compos. Part B Eng.* **2018**, *150*, 7–13. [CrossRef]
88. Lu, J.; Zhang, W.; Huo, W.; Zhao, Y.; Cui, W.; Zhang, Y. Electrochemical Corrosion Behavior and Mechanical Properties of Nanocrystalline Ti–6Al–4V Alloy Induced by Sliding Friction Treatment. *Materials* **2019**, *12*, 760. [CrossRef]
89. Fayazfar, H.; Salarian, M.; Rogalsky, A.; Sarker, D.; Russo, P.; Paserin, V.; Toyserkani, E. A Critical Review of Powder-Based Additive Manufacturing of Ferrous Alloys: Process Parameters, Microstructure and Mechanical Properties. *Mater. Des.* **2018**, *144*, 98–128. [CrossRef]
90. Jablokov, V.; Goto, D.M.; Koss, D.A.; McKirgan, J.B. Temperature, Strain Rate, Stress State and the Failure of HY-100 Steel. *Mater. Sci. Eng. A* **2001**, *302*, 197–205. [CrossRef]
91. Deb, P.; Challenger, K.D.; Therrien, A.E. Structure-Property Correlation of Submerged-Arc and Gas-Metal-Arc Weldments in HY-100 Steel. *Metall. Mater. Trans. A* **1987**, *18*, 987–999. [CrossRef]
92. Lunde, J.; Kazemipour, M.; Salahi, S.; Nasiri, A. Microstructure and Mechanical Properties of AISI 420 Stainless Steel Produced by Wire Arc Additive Manufacturing. In Proceedings of the TMS 2020 149th Annual Meeting & Exhibition Supplemental Proceedings, San Diego, CA, USA, 23–27 February 2020; pp. 413–424. [CrossRef]
93. Guha, R.D.; Sharma, A.J.; Diwan, P.; Khanikar, P. Effect of Grain Orientation on High Strain-Rate Plastic Deformation. *Procedia Eng.* **2017**, *173*, 1048–1055. [CrossRef]

94. Salahi, S.; Nemani, A.V.; Ghaffari, M.; Lunde, J.; Nasiri, A. On Microstructure, Crystallographic Orientation, and Corrosion Properties of Wire Arc Additive Manufactured 420 Martensitic Stainless Steel: Effect of the Inter-Layer Temperature. *Addit. Manuf.* **2021**, *46*, 102157. [CrossRef]
95. Khodabakhshi, F.; Farshidianfar, M.H.; Gerlich, A.P.; Nosko, M.; Trembošová, V.; Khajepour, A. Effects of Laser Additive Manufacturing on Microstructure and Crystallographic Texture of Austenitic and Martensitic Stainless Steels. *Addit. Manuf.* **2020**, *31*, 100915. [CrossRef]
96. Vahedi Nemani, A.; Ghaffari, M.; Salahi, S.; Nasiri, A. Effects of Post-Printing Heat Treatment on the Microstructure and Mechanical Properties of a Wire Arc Additive Manufactured 420 Martensitic Stainless Steel Part. *Mater. Sci. Eng. A* **2021**, *813*, 141167. [CrossRef]
97. Nagaraju, K.V.V.; Kumaran, S.; Rao, T.S. Electrochemical Behavior of Various Grade P/M Stainless Steels Processed by Rapid Microwave Hybrid Sintering (Super-Solidus) Method. *Mater. Lett.* **2021**, *302*, 130394. [CrossRef]
98. Alonso-Falleiros, N.; Wolynec, S. Correlation between Corrosion Potential and Pitting Potential for AISI 304L Austenitic Stainless Steel in 3.5% NaCl Aqueous Solution. *Mater. Res.* **2002**, *5*, 77–84. [CrossRef]
99. Loto, R.T. Pitting Corrosion Resistance and Inhibition of Lean Austenitic Stainless Steel Alloys. In *Austenitic Stainless Steels—New Aspects*; IntechOpen: London, UK, 2017. [CrossRef]
100. Isfahany, A.N.; Saghafian, H.; Borhani, G. The Effect of Heat Treatment on Mechanical Properties and Corrosion Behavior of AISI420 Martensitic Stainless Steel. *J. Alloys Compd.* **2011**, *509*, 3931–3936. [CrossRef]
101. Singh, M.; Shahi, A.S.; Singh, D. Influence of Heat Input on the Pitting Corrosion and Tensile Behavior of GTA Welded Martensitic Stainless Steel (AISI410 SS) Joints. *Mater. Today Proc.* **2021**, *46*, 10282–10287. [CrossRef]